Pharmaceutical Research, Vol. 27, No. 5, May 2010 (© 2010)
DOI: 10.1007/s11095-010-0078-x

Research Paper

Magnetic Deposition of Aerosols Composed of Aggregated Superparamagnetic Nanoparticles

Yuanyuan Xie,[1] Pengyun Zeng,[1] Ronald A. Siegel,[4] Timothy Scott Wiedmann,[1] Bruce E. Hammer,[2] and P. Worth Longest[3,5]

Received October 12, 2009; accepted February 2, 2010; published online March 3, 2010

Purpose. The deposition of magnetic particles was examined for the possibility of further enhancing the selectivity of inhalation drug administration for the treatment of lung cancer.
Methods. Superparamagnetic magnetite nanoparticles were prepared and ultrasonically atomized, dried, and passed through glass tubes in the presence and absence of a wedge-shaped permanent magnet. The change in the outlet aerosol size distribution due to magnetic deposition under various well-defined aerodynamic conditions and a measured magnetic field was determined by an aerodynamic particle sizer. In addition, computational fluid dynamics (CFD) simulations of magnetic aerosol transport and deposition were conducted.
Results. The deposition fraction increased nearly linearly with particle diameter and was greater with lower air flow rates. The effect of tube diameter was complicated but well described by CFD simulations, as was the effect of particle size and air flow rate.
Conclusions. The descriptive power of CFD simulations was demonstrated in the *in vitro* deposition of magnetic aerosol particles. This suggests that CFD simulations can potentially be used in future studies to design systems for selective drug delivery *in vivo* as a function of magnetic properties, aerosol characteristics, and respiratory physiology.

KEY WORDS: computational fluid dynamics; magnetic particle deposition; magnetite; respiratory drug delivery; targeted aerosol deposition.

INTRODUCTION

Aerosol particles composed of magnetite nano-spheres have several useful properties for applications in respiratory drug delivery (1–5). First, superparamagnetic nanoparticles (SPNP) may be detected by magnetic resonance imaging, which has potential for providing diagnostic information (3,4,6). Second, the particle trajectories in the airways can be modified by a non-invasive external magnetic field gradient (1,7,8). Third, they can be heated with an external alternating magnetic field (9). Fourth, the surface of the aerosol can be modified with ligands, thereby targeting the particle to specific cells (5,10,11). Finally, they do not pose significant safety concerns, because they are composed of simple iron oxides that are biodegradable and have been previously implemented as diagnostic agents in imaging the lung (3).

Our interest in magnetic particles arose from the possibility of further enhancing the selectivity of inhalation drug administration for the treatment of lung cancer. Previously, Brain *et al.* (12) successfully enhanced the deposition of magnetic particles in rabbits using an iron oxide aerosol and an external magnetic field gradient. More recently, an *in vitro* study has been conducted where the deposition fraction of aerosol particles was determined in a magnetic field (13). An *in vitro* study has also illustrated the enhanced deposition of high aspect ratio aerosols in small airways using magnetic field alignment (14). In a recent animal study, magnetic aerosol droplets were localized to the upper lobe of a mouse lung, thereby demonstrating the potential of spatially targeting deposition *in vivo* (15). Here, we examine the change in the outlet aerosol size distribution due to magnetic deposition under various well-defined aerodynamic conditions and a measured magnetic field. In addition, computational fluid dynamics (CFD) simulations of magnetic aerosol transport and deposition are conducted and compared with the experimental findings. The CFD simulations are used to highlight transport and deposition details not observed in the

[1] Department of Pharmaceutics, University Of Minnesota, Minneapolis, Minnesota, USA.
[2] Department of Radiology, University Of Minnesota, Minneapolis, Minnesota, USA.
[3] Department of Mechanical Engineering and Department of Pharmaceutics, Virginia Commonwealth University, 401 West Main Street, P.O. Box 843015 Richmond, Virginia 23284-3015, USA.
[4] Department of Pharmaceutics and Department of Biomedical Engineering, University Of Minnesota, Minneapolis, Minnesota, USA.
[5] To whom correspondence should be addressed. (e-mail: pwlongest@vcu.edu)

ABBREVIATIONS: APS, Aerodynamic particle sizer; CFD, Computational fluid dynamics; exp, Experimental results; id, Internal diameter; LPM, Liters per minute; UFD, User-defined function.

0724-8741/10/0500-0855/0 © 2010 Springer Science+Business Media, LLC

experiments and may be used in future analysis to engineer the targeted deposition of magnetic aerosols in the lung.

THEORY

Force on a Magnetic Particle

The force on a magnetic particle due to an externally applied magnetic field can be expressed as

$$\vec{F}_m = \vec{\nabla}\left(\vec{M} \cdot \vec{B}\right) \quad (1)$$

where the force, $\vec{F}$, is in Newtons (N), $\vec{M}$ is the induced magnetic moment vector in amperes meters squared ($A{\cdot}m^2$), $\vec{B}$ is the magnetic flux density vector in Tesla (T), and $\vec{\nabla}$ is the grad operator (1/m). Based on the coordinate system shown in Fig. 1 and the assumption that the magnetic field is constant down the length of the magnet, changes in y and the y-component of the $\vec{B}$ vector can be neglected. The resulting force term in Cartesian coordinates becomes

$$\vec{F}_m = \frac{\partial}{\partial x}(M_x B_x + M_z B_z)\hat{i} + \frac{\partial}{\partial z}(M_x B_x + M_z B_z)\hat{k} \quad (2)$$

where M_i and B_i are the components of the magnetic moment and flux density vectors in the generalized *i*-direction. Unit vectors in the x and z directions are expressed as $\hat{i}$ and $\hat{k}$, respectively. In this equation, the magnetic moments are also functions of the field intensity, i.e., $M_i{=}f\,(B_i)$. However, for a given change in B_i, the change in M_i is often significantly less. As a result, the equation above can be simplified by assuming that M_i is locally constant. The magnetic force equation becomes

$$\vec{F}_m = \left(M_x \frac{\partial B_x}{\partial x} + M_z \frac{\partial B_z}{\partial x}\right)\hat{i} + \left(M_x \frac{\partial B_x}{\partial z} + M_z \frac{\partial B_z}{\partial z}\right)\hat{k} \quad (3)$$

In this expression, the magnetic moment vector components in each vector direction (*i*) can be determined as

$$M_i = M_i^* \cdot m_{Mag} \quad (4)$$

The term M_i^* is the magnetic moment *i*-component per unit mass of magnetite (m_{Mag}) in the particle, which is a function of the applied magnetic flux density, B_i. The resultant force may be determined from the experimentally accessible parameters of the observed magnetic field, particle mass, and the induced magnetic moment of magnetite per unit mass.

MATERIALS AND METHODS

Ferrous chloride tetrahydrate ($FeCl_2{\cdot}4H_2O$) and ferric chloride hexahydrate ($FeCl_3{\cdot}6H_2O$) were purchased from Fluka. Ammonium hydroxide (29%) was purchased from Fisher Scientific (Minneapolis, MN).

Magnetite Nanoparticle Synthesis and Characterization

Magnetite nanoparticles were synthesized by chemical coprecipitation of $FeCl_3$ and $FeCl_2$ by the addition of an alkaline solution (16). Generally, 0.30 g $FeCl_2{\cdot}4H_2O$ (1.5 mmole) and 0.82 g $FeCl_3{\cdot}6H_2O$ (3.3 mmole, 10% excess) were dissolved in 20 ml distilled and deionized water, which was previously deoxygenated by alternating between bubbling with argon gas and placing under house vacuum. To the iron chloride solution, 2 ml ammonium hydroxide was added. The resulting black precipitate was centrifuged at 480 rpm for 5 min. The supernatant was decanted from the precipitate, and the particles were washed with pH 2 HCl solution followed by centrifugation. The supernatant was removed again, and particles were washed once in pH 3 HCl solution and centrifuged, and the pellet was suspended in pH 3 HCl. The remaining chloride concentration was estimated by measuring the electrical conductivity. The iron content was determined by measuring the absorbance following solubilizing with pH 2 HCl and complexing with phenathroline using appropriate standards. The nanoparticle size distribution in an aqueous dispersion was determined by dynamic light scattering (Nicomp submicron particle sizer, model 370, Pacific Scientific Hiac/Royco Instruments Division, Santa Barbara, CA) and found to have a mean diameter of 16.8± 3.2 nm. An image of the aggregated particles after aerosolization from an S-900 SEM system is shown in Fig. 2. As can be observed in the image, the nanoparticles have a generally spherical shape and are aggregated into larger microparticles.

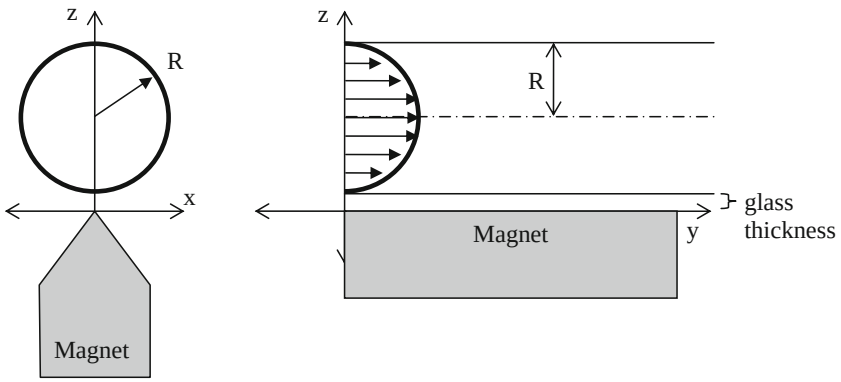

Fig. 1. Experimental system for magnetic deposition, including coordinates and position of the magnet. The glass tubes were 1 mm thick in most cases, resulting in a gap between the tip of the magnet and the inner surface of the geometry.

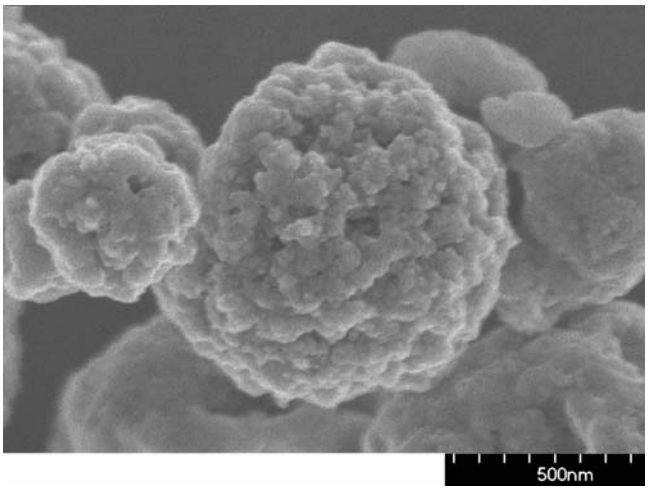

Fig. 2. Scanning electron micrograph of aggregate nanoparticles viewed after coating with 1–2 nm of platinum.

Magnetic Field and Induced Moment

The spatial dependence of the magnetic field was determined by a Hall effect magnetometer. The induced magnetization and saturation magnetization values of vacuum dried Fe_3O_4 were measured with a Vibrating Sample Magnetometer (Lakeshore 7400 Series VSM system, Westerville, OH) at 298 K. The measured moments were corrected using a Ni standard sample with a typical precision of 2%.

Aerosol Generation and Deposition

For particle generation, a Pyrex glass baffle was constructed (47 mm diameter, University of Minnesota, Department of Chemistry Glass Shop) and placed in the water bath, directly over the ultrasonic transducer (17). A 1.7 MHz transducer (Mainland Mart, mainlandmart.com) was used to generate the initial droplets from the aqueous dispersion of magnetite particles. The droplets were entrained by the air and carried through a stainless steel reflux drying column that had outer column and inner condenser temperatures maintained at 105 and 5°C, respectively. The resulting dried particles were passed through a U-tube, which directed the aerosol upward through diameter-reducing flow connections, and finally into a cylindrical glass tube of variable diameter that had an external wedge-shaped permanent magnet (Alnico) positioned parallel to its longitudinal axis. A stir bar was also included upstream of the glass tubes to ensure adequate mixing of the particle concentration field after passage through the 180° bend. Control experiments were conducted in the same manner without the magnet. Following passage through the tube, the particles were diluted with air and then directed into an aerodynamic particle sizer (APS, TSI, Minneapolis, MN). The outlet aerosol size distribution was determined relative to a control experiment in which the magnet was removed. Four different tubes were used with diameters of 2, 4, 6, and 12.7 mm, and the flow rate was varied between 0.2 and 0.5 LPM.

Flow Field and Particle Trajectory Solutions

Computational fluid dynamics (CFD) simulations of magnetic aerosol transport and deposition were conducted. A simple model was considered that consisted of magnetite particles in a cylindrical tube with radius R in conjunction with a wedge-shaped magnet with its edge positioned along the y-axis, parallel to the tube length (Fig. 1). Systems considered with the CFD model were consistent with the *in vitro* experiment and included internal tube diameters from 2 to 12.7 mm and flow rates from 0.2 to 0.5 LPM. The glass thickness was approximately 1 mm, and the length of the tubes was 100 mm. The wedge-shaped magnet had a total length of 34 mm and was positioned in a central section of the glass tube. As a result, the glass tube geometry consisted of a 33 mm inlet section, the 34 mm magnetic zone, and a 33 mm outlet. The magnetic field was assumed to only vary in the x and z directions (Fig. 1) and to be constant along the length of the magnet, i.e., fringe effects were neglected.

The Reynolds numbers of the tubular geometries ranged from approximately 21 to 300, indicating fully developed laminar flow. Considering the use of diameter-reducing flow connections and a stir bar leading to the glass tubes in the *in vitro* system, uniform inlet velocity profiles were assumed to enter the 100 mm glass tubes, which was the beginning of the numerical model. The low Reynolds numbers and small diameters ensured that the flow was nearly fully developed at the start of the axially oriented magnet. The isothermal laminar and incompressible flow fields of interest were simulated using the CFD package Fluent 6.3 (Ansys, Inc.). To ensure solution accuracy, hexahedral mesh elements were employed, and grid convergence of the flow field was verified (18).

In previous studies, Lagrangian particle tracking was shown to accurately and effectively predict the local and total deposition of nano- and micro-aerosols (19,20). The Lagrangian equation describing the transport and deposition of magnetic aerosols can be written

$$\frac{dv_i}{dt} = \frac{f}{\tau_p}(u_i - v_i) + g_i(1-\alpha) + f_{Brownian,\,i} + f_{M,\,i} \text{ and}$$
$$\frac{dx_i}{dt} = v_i(t) \tag{5}$$

Here, v_i and u_i are the components of the particle and local fluid velocity, respectively. The characteristic time required for a particle to respond to changes in fluid motion, or the particle relaxation time, is expressed as $\tau_p = C_c \rho_p \, d_p^2/18\mu$, where C_c is the Cunningham correction factor for submicrometer aerosols, and μ is the absolute viscosity of the continuous phase. The gravity vector, g_i, was oriented along the longitudinal axis of the tube opposite the direction of flow. The effect of Brownian motion on the trajectories of submicrometer particles was included as a separate force per unit mass term at each time-step (19). The drag factor, f, which represents the ratio of the drag coefficient to Stokes drag, was based on the expression of Morsi and Alexander (21). Finally, the term $f_{M,i}$ represents the force per unit mass on the magnetic aerosols of interest in this study, as shown in Eq. 3, divided by the particle mass.

Solution of the particle trajectory equation was accomplished by a combination of the particle trajectory algorithm

in Fluent 6.3 and a user-defined function (UDF) for the calculation of the magnetic force term. Briefly, a UDF was written to evaluate the magnetic force per unit mass at each particle time-step throughout the flow domain. Based on experimental measurements, the magnetic flux density components B_x and B_z of the externally applied field were entered in the UDF explicitly. Gradients of these fields were calculated using second-order central differences. At each time step, the local magnitude of the magnetic density in the vicinity of the particle was used in conjunction with experimental measurements to calculate the total magnetic moment. Magnetic moments in each direction were then based on unit vectors calculated from the B_x and B_z components. The magnetic gradients in the x and z directions were calculated to produce the magnetic force on the particle, based on Eq. 3. A variable time-step-size accuracy control routine was implemented to ensure efficiency and accuracy of the trajectory solution (22). For each aerosol size class considered, approximately 3,000 particles were simulated. Doubling the number of simulated particles had a negligible effect (<1%) on the deposition fraction predictions for all cases. Aerosols were initialized using a constant profile at the inlet of the 100 mm glass tube, and deposition fractions were based on the number of particles contacting the wall within the 34 mm magnetic region.

RESULTS

In preparation for determining the magnetic deposition, the spatial dependence of the magnetic field as a function of direction was determined for the wedge-shaped magnet. The results are given in Fig. 3. The field strength directed towards the magnet (B_z) was large and symmetric about the edge of the magnet (Fig. 3a). Moving away from the magnet in the z-direction, the B_z component of field strength decreased rapidly initially as indicated by the closely spaced contour lines. This rapid decrease in field strength produced high spatial gradients, which create the strongest magnetic forces of this field, as predicted by Eq. 3. The x-direction magnetic density (B_x) was near zero along a plane perpendicular to the x-axis in the center of the field (Fig. 3b). Moving in the x-direction, the B_x term increases initially and then decreases. In general, the z-component of magnetic density was approximately 5 to 10 times greater than the x-component. Considering both magnetic components together, the area-averaged magnetic density for the 2 mm tube was in the range of 0.2–0.25 T. In comparison, the area-averaged magnetic density in the 12.7 mm tube was approximately 0.05–0.1 T.

As a result of magnetic forces, particles are expected to move in a direction perpendicular to the lines of constant magnetic density shown in Fig. 3. Considering that the B_z component of magnetic density is significantly stronger, this field will control the direction of particle motion. As a result, particle trajectories are expected to curve inward toward the tip of the wedge-shaped magnet.

The induced moment for the magnetite nanoparticles was also measured as a function of the applied field, and the results are given in Fig. 4. The moment rose rapidly with small changes in the applied field, but reached a saturation value near 80 A m^2/kg (emu/g), consistent with the literature

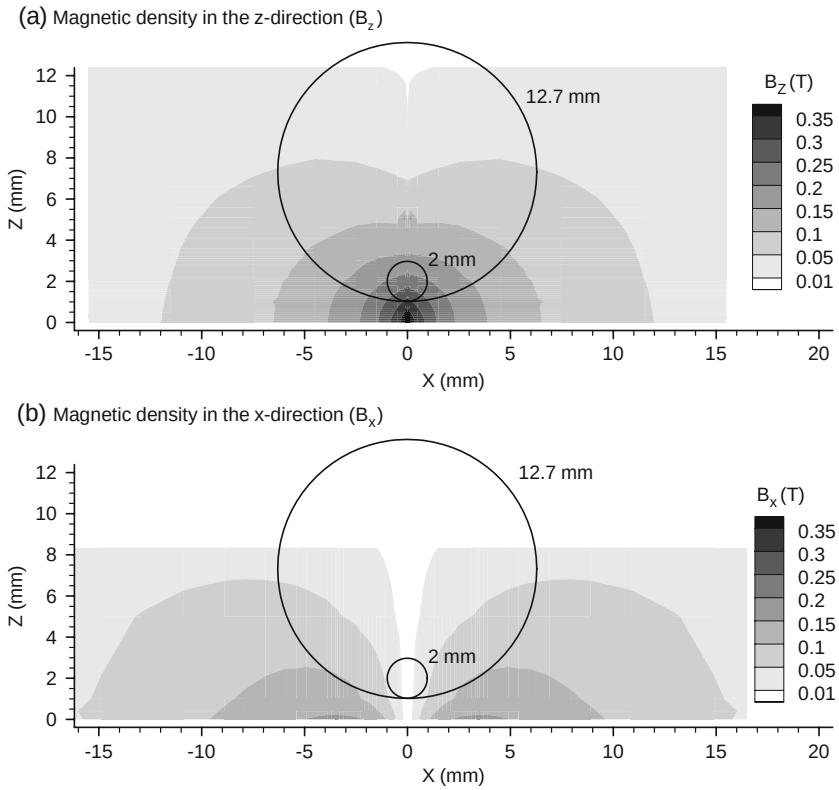

Fig. 3. Spatial distribution of the magnetic density vector components (**a**) B_z and (**b**) B_x. These values are based on experimental measurements, which were smoothed into a continuous field using linear interpolation.

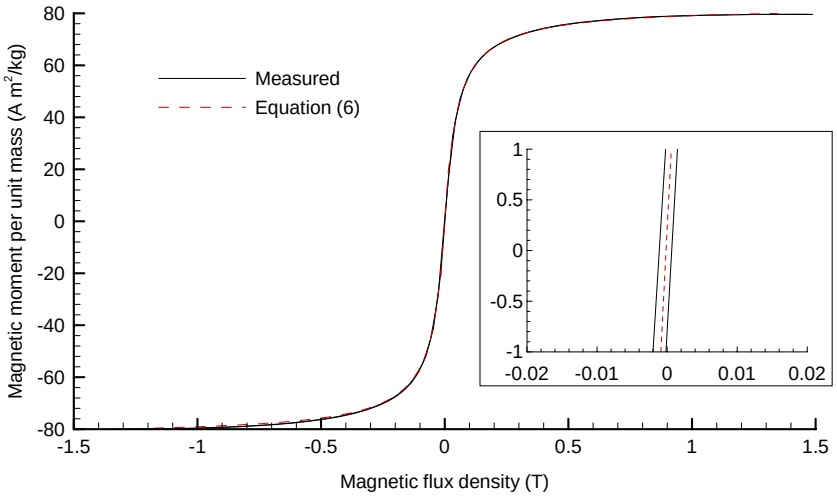

Fig. 4. Induced magnetic moment per unit mass as a function of applied magnetic field. The panel insert shows a minimal hysteresis in the measured data and good agreement with the best fit curve reported as Eq. 6.

value of magnetite (23). In the figure, the absence of a visible hysteresis indicates that the material is superparamagnetic. Only a small separation of the experimentally measured magnetic moment curves is observed in the inserted panel of Fig. 4, which represents a magnification of approximately 70X.

To match the experimental measurements, the following expression was developed for the magnetic moment per unit mass of dried magnetite particles

$$M^* = \frac{\left|\vec{B}\right|(10^4)}{a\left|\vec{B}\right|(10^4) + b} \tag{6}$$

where a=1.22×10^{-2} kg/Am^2, b=5.62 kgT/Am^2, M_i^* has units of A·m^2/kg (emu/g), and $\left|\vec{B}\right|$ is the magnitude of the flux density vector in units of T. The 10^4 term is used to convert Tesla (the standard SI unit of flux density) to Gauss (which is typically measured) in the equation. In Eq. 6, it is important to evaluate the magnetic moment per unit mass based on the total magnitude of the flux density vector such that the magnetic saturation of the material is not exceeded. The magnetic moments per unit mass in each coordinate direction for use in Eq. 4 can then be calculated as

$$M_i^* = M^* \frac{ABS(B_i)}{\left|\vec{B}\right|} \tag{7}$$

where ABS(B_i) is the absolute value of the magnetic density vector component in the *i*-direction.

In Fig. 4, a good match is observed between the measured magnetic moment curve and the approximate correlation. Considering average magnetic densities in the 2 and 12.7 mm tubes of 0.225 and 0.75 T, as shown in Fig. 3, the associate magnetic moments per unit mass are 68.6 and 51.1 A m^2/kg (emu/g), respectively, which are below the saturation value.

The mass concentrations of the aerosol particles for the control and magnetic experiments are given in Fig. 5 as determined by the APS. The divergent distributions reflect the deposition fraction of magnetic particles, which was greater for the larger particle sizes. In these experiments, a black deposited mass on the glass surface of the tube was clearly evident. The data was collected in triplicate and in general was quite reproducible with standard deviations of 5% or less. This substantiates the magnetic deposition of an aerosol composed of nanoparticles.

In Fig. 6, the deposition fraction is given as a function of aerodynamic particle size for four airflow rates. The deposition fraction increased nearly linearly with increasing particle size, and at sizes over 2 μm, almost complete deposition was observed. Deposition fractions for sizes below 1 μm tended to be less reliable due to the lower values and inability of the laser diffraction methodology to characterize this size range. Here it can be seen that increasing the flow rate caused a

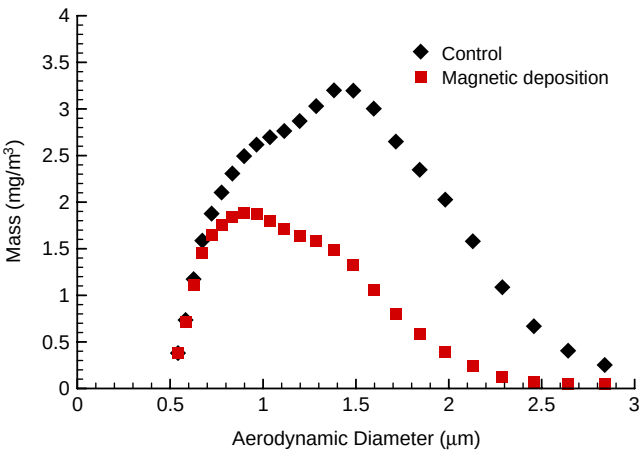

Fig. 5. Mass concentration given as a function of particle size for (♦) control and (■) magnetic deposition cases determined at a flow rate of 200 ml/min and a tube size of 4 mm (id) using an APS.

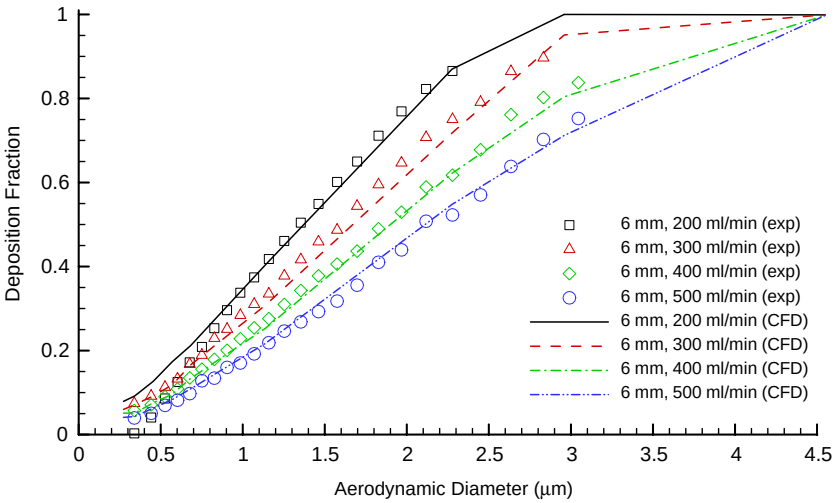

Fig. 6. Deposition fraction given as a function of aerodynamic particle size in a 6 mm tube at flow rates of (□) 200, (Δ) 300, (◊) 400 and (○) 500 ml/min. The *solid lines* represent simulations using the CFD model.

corresponding decrease in the deposition fraction for a single tube size.

Model predictions of aerosol deposition as a function of aerodynamic size and flow rate are also compared with the experimental results in Fig. 6. As observed in the figure, the CFD predictions match the *in vitro* results to a high degree for all flow rates considered and nearly all particle sizes. One exception is the disparity between the predictions and experimental results for a flow rate of 200 ml/min and aerodynamic diameters less than approximately 0.75 μm. In this range, the CFD predictions are consistent in trend with the results of other flow rates. In contrast, the experimental results at 200 ml/min and particle sizes less than 0.75 μm are the lowest reported values, which is not consistent with the trend of increasing deposition as the flow rate is reduced.

In Fig. 7, analogous experiments were carried out with the APS to examine the effect of tube size on deposition. As before, an approximately linear dependence of the deposition on particle size is shown. In general, the effect of tube size was modest. The interesting finding was that for small particle sizes, the highest deposition fraction was observed with the 12.7 mm tube, but for large particle sizes, the highest deposition was observed with the 4 mm tube.

Model predictions of deposition as a function of tubular size are also shown in Fig. 7 compared with experimental data. In general, the CFD simulations qualitatively capture the rank order of deposition as a function of tube size for different aerodynamic diameters. For example, at the largest aerodynamic diameter considered, highest to lowest deposition was observed for the 4, 6, 2 and 12.7 mm tubes. The CFD model predicted highest to lowest deposition for tubular diameters of 6, 4, 12.7 and 2 mm. These rankings highlight two critical factors in magnetic aerosol deposition, which are (i) flow rate and (ii) strength of the magnetic field and magnetic gradient (i.e., magnetic forces). These factors are both favorable for higher deposition in the 6 and 4 mm tubes.

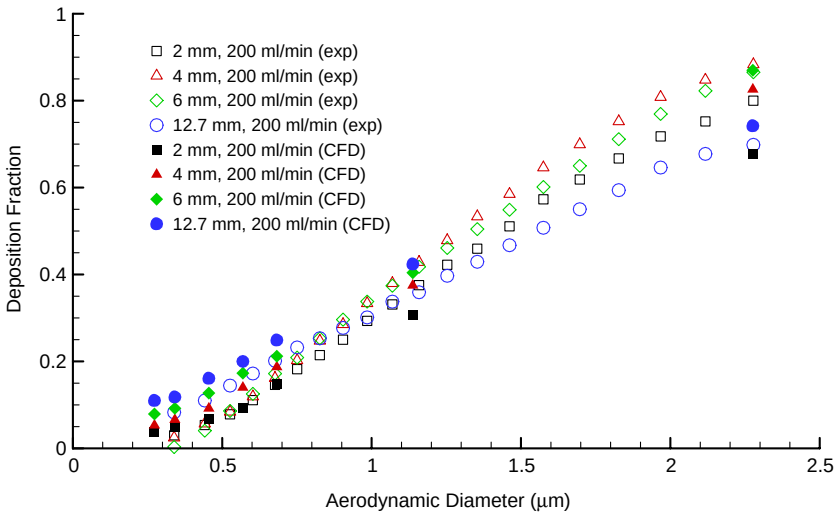

Fig. 7. Deposition fraction given as a function of aerodynamic particle size for tube internal diameters of (□) 2, (Δ) 4, (◊) 6, and (○) 12.7 mm using a flow rate of 200 ml/min. The *filled symbols* represent simulations using the CFD model.

In contrast, increasing the flow rate, as occurs with the 2 mm tube, or decreasing the field and gradient strength, as occurs with the 12.7 mm tube, can each reduce deposition at the largest aerosol size considered. The fact that this rank order changes for smaller particle sizes indicates a complex interplay among the factors of flow rate, magnetic field strength, tubular diameter, particle mass, and drag.

In Fig. 8, longitudinal and cross-sectional views are given for the trajectories of magnetic particles with a geometric diameter of approximately 2 μm in the 6 mm and 12.7 mm tubes at a flow rate of 200 ml/min. Considering the cross-sectional view for each tube, the particle trajectories appear to curve away from the tube center in the upper half of the geometry and move toward the magnet tip in the lower half. This pattern is consistent with the magnetic density field in the z-direction, as shown in Fig. 3a. As described, the magnetic force acts to move the particles perpendicular to the lines of constant magnetic density.

In the longitudinal views of Fig. 8, the magnetic field is observed to affect nearly all particle trajectories. As expected, the secondary velocities (v_x and v_z) increase as the particles approach the magnet. These secondary velocity components can exceed the axial velocity, resulting in trajectories that move nearly perpendicular to the wall. Ratios of secondary-to-axial velocity above one are observed near the magnet and along the lower perimeter of both tubular geometries. Furthermore, a larger region where the secondary velocity values are above one is observed for the larger geometry, due to the reduced axial flow rate. Therefore, higher deposition might be expected in the larger geometry despite the reduction in average magnetic field strength. However, Fig. 7 indicates that lower deposition is observed for a 2 μm particle in the 12.7 mm geometry compared with the 6 mm model. This discrepancy can be explained by the fact that the particles in the larger tube must travel further before depositing compared with the smaller tube. As a result, tube

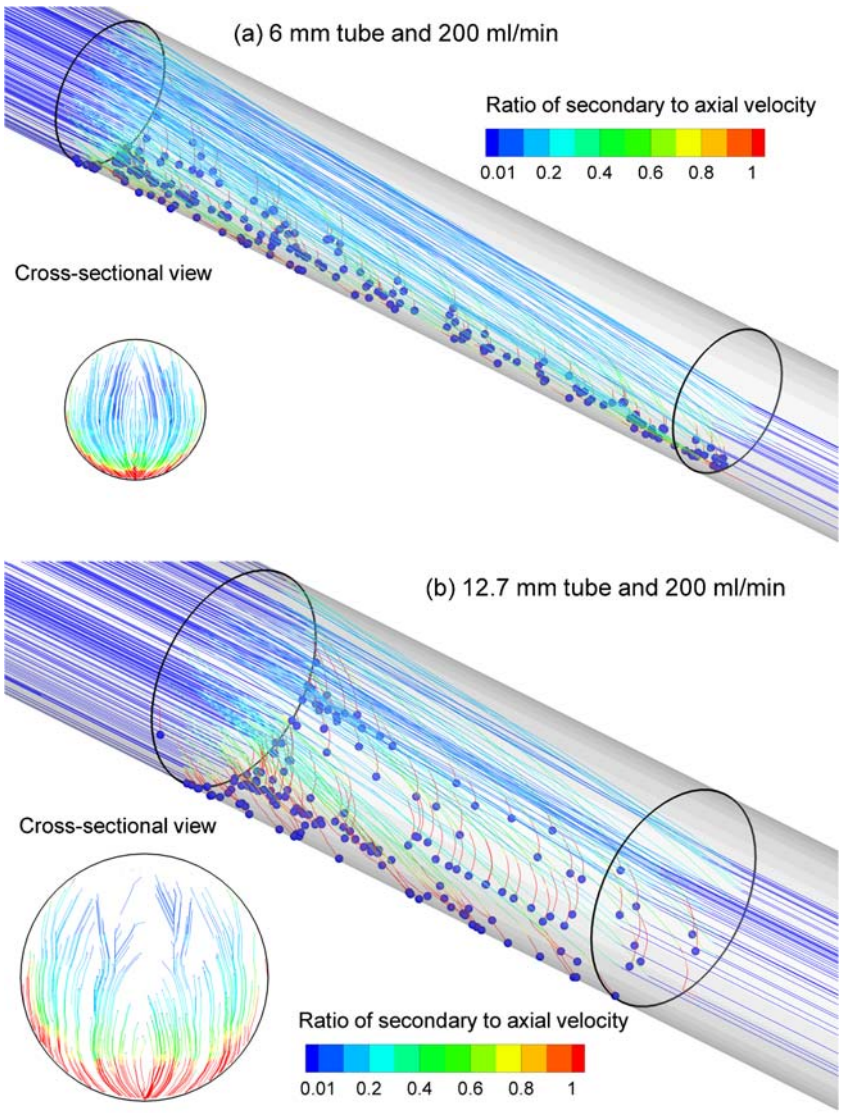

Fig. 8. Trajectories of particles within a 2 μm aerodynamic diameter at a flow rate of 200 ml/min in the (**a**) 6 mm and (**b**) 12.7 mm internal-diameter tubes. The trajectories are colored according to the ratio of secondary (v_z and v_x) to axial (v_y) velocity.

diameter appears to affect both the flow rate (or residence time) aspect of particle deposition as well as the distance required for the particle to travel before deposition occurs. This two-fold influence of tube diameter may help to explain why no one tubular diameter in Fig. 7 was observed to have the highest deposition fraction across all particle sizes considered.

Deposition in the 6 mm tube with a flow rate of 200 ml/min is illustrated in Fig. 9 based on the *in vitro* experiments and numerical model results. The image of *in vitro* deposition shows outlines of the outer and inner tubular surfaces with deposition in the lower quarter of the cross-sectional perimeter, which was nearest the magnet. It is noted that the magnet was positioned with the tip in the middle of the shaded deposition region. Numerical simulation predictions for a polydisperse aerosol based on the experimental distribution shown in Fig. 5 are presented in Fig. 9b. In this figure, the tube is oriented to facilitate comparison with the *in vitro* image shown in Fig. 9a. For a direct visual comparison to the experimental results, numerical deposition locations are represented as single gray pixels (Fig. 9b). It is observed that the predicted deposition resides in the lower quarter of the cross-sectional perimeter, as with the experiment. While the images are not exactly to scale, fringe effects of the magnetic field in the axial direction may be responsible for the less defined beginning and end of the magnetic deposition zone observed in the experimental results. In contrast, a very sharp beginning and end of the magnetic zone are observed in the numerical figure. Alternatively, some particle rolling after deposition as well as the collected mass of deposited nanoparticles may blur the *in vitro* deposition region of the experiment.

Numerical predictions of deposition as a function of particle size are illustrated in Fig. 9c. A slightly higher proportion of larger aerosols are observed to deposit in the upstream (left) portion of the magnetic zone. Still, the distribution of particle sizes appears to be nearly uniform and along the lower quarter of the cross-sectional perimeter as observed experimentally. These results help to illustrate the predictions of highly localized magnetic particle deposition as a function of particle size that are possible with the CFD model developed in this study.

DISCUSSION

Magnetic particles offer a number of desirable features, particularly in the area of theranosis—that is, a delivery system that provides a means to diagnosis as well as treat

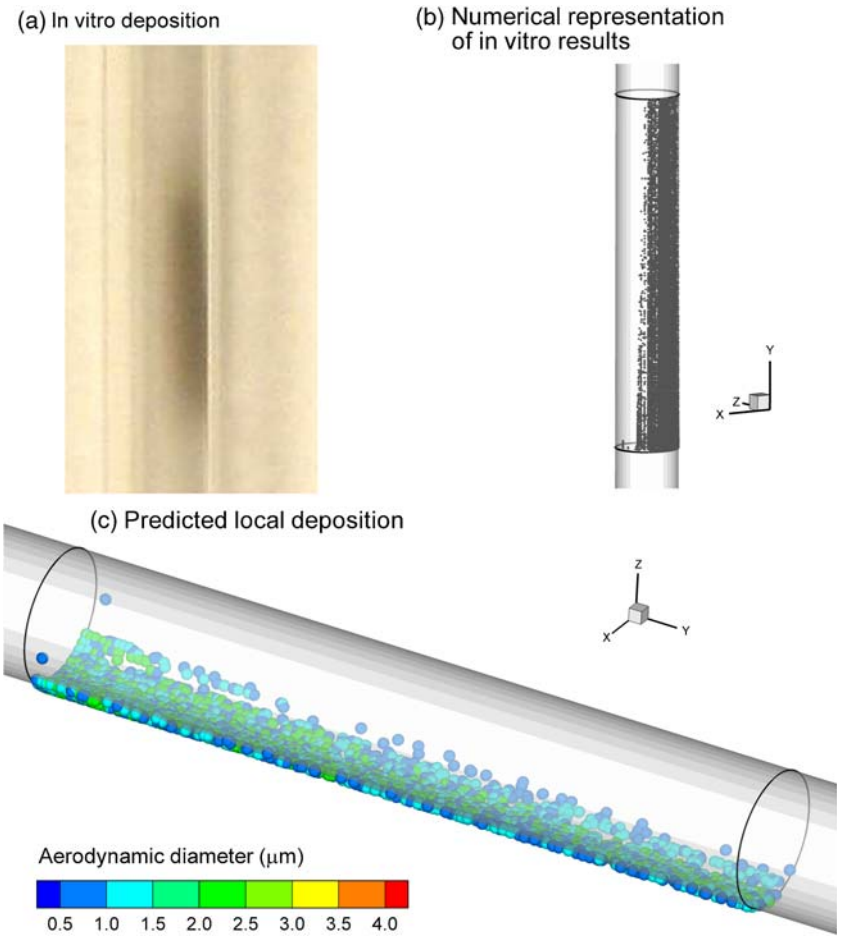

Fig. 9. Deposition in the 6 mm (id) tubular geometry at a flow rate of 200 ml/min based on the (**a**) *in vitro* experiment and (**b** & **c**) numerical simulations. The model results shown in panel **b** predict a similar shading pattern to the *in vitro* results of panel **a**. As shown in panel **c**, the numerical results can also predict the local deposition patterns of individual particle sizes for the polydisperse aerosol.

disease. This concept perhaps can be more readily realized with inhalation, since the respiratory tract is readily accessible. In the treatment of lung cancer, control of the site of delivery would be advantageous, and this work provides the foundation for understanding and predicting the respiratory deposition of magnetic particles.

The magnetic particle dispersion was prepared by closely following the Massart procedure (16). Specialized mixing or sonication was found not to be useful in preparing a stable colloidal dispersion, but rather, the critical factor appeared to be the addition of a slight excess of either Fe^{3+} or Fe^{2+}. The rinsing process was effective in reducing the counterion concentration to a minimum, since the final conductivity was typically less than 1 mmho. This would correspond to a chloride concentration of 1 mM, assuming no other ion contributed to the conductivity. The particle size distribution of the aqueous dispersion prior to atomization had a number mean size of 200±50 nm. This represents the size of individual particles with initial diameters of approximately 20 nm, that are aggregated into larger particles. This dispersion sediments with time and could not be atomized after 3 or 4 days of storage at room temperature. It appears there is continued aggregate growth, which, upon reaching micrometer-sized aggregates, interferes with the ultrasonic atomization process. As such, dispersions were used within 2 days of preparation.

Theoretically, the magnetically induced velocity of the aerosol particles depends on the magnetic moment and field gradient. Each particle has a specific value for the moment at any point within the magnetic field. For the simulation of the magnetic deposition, the particle size distribution and induced moment of a bulk sample were experimentally determined to allow calculation of the spatial dependence of the induced moment of any given particle. Moreover, the magnetic field of the wedge-shaped magnet was measured in the vicinity where the glass tubes were positioned out through near zero magnetic density. The two components (x, z) of the axially symmetric magnetic field were used in the CFD simulations from which the spatially dependent induced magnetic moment and the magnetic field gradients were calculated.

In Eq. 4, the mass of magnetite in the particle (m_{Mag}) was estimated as

$$m_{Mag} = \rho_{Mag} V_{Mag} = \rho_{Mag}(\alpha_{Mag} V_p) = \rho_{Mag}\alpha_{Mag}\left(\frac{\pi d_p^3}{6}\right) \quad (8)$$

In the expression above, the subscript p indicates composite particle properties, ρ represents density, V is volume, and α_{Mag} is the volume fraction of magnetite in the particle. Magnetite aerosols appeared as aggregates in scanning electron microscope images. This is consistent with the method of formation in which aerosol droplets containing a dispersion of nanoparticle spheres with diameters of approximately 20 nm were evaporated (24). The volume packing fraction of the constituent magnetite spheres forming the aggregate particles is most likely between the random close (α=0.64) (25) and crystalline (α=0.74) (25) packing fractions. In this study, a crystalline close packing fraction was assumed such that α_{Mag}=0.74.

To calculate particle trajectories, the magnetic force is needed per unit particle mass. As described, the particles are assumed to be composed of aggregated nano-spheres. Furthermore, these particles are suspended in an aqueous solution for aerosolization. It is assumed that water on the surface of the aggregate particle is fully evaporated; however, water within the aggregate pores (~1 nm scale) does not evaporate due to molecular attraction. As a result, the particles are composed of nanoscale magnetite spheres with interstitial water. The resulting composite density of these particles is

$$\rho_p = \rho_{Mag}\alpha_{Mag} + \rho_{H_2O}(1 - \alpha_{Mag}) \quad (9)$$

The particle mass is then calculated as

$$m_p = \rho_p V_p \quad (10)$$

where a spherical particle geometry is assumed in evaluating the particle volume. The particle aerodynamic diameter (d_{ae}), for comparison with experimental deposition measurements, is calculated as

$$d_{ae} = d_{geo}\left(\frac{\rho_p}{\rho_{H_2O}}\right)^{1/2} \quad (11)$$

The density of magnetite was assumed to be 5,180 kg/m^3, and the density of water was assumed to be 1,000 kg/m^3, resulting in an expression d_{ae}=d_{geo} × 1.92.

In the computational analysis, the value of the induced magnetic velocity was calculated at each point in space, which then was used to determine the displacement in a finite time. It should be noted that the cross terms of the magnetic field gradient (dB_x/dz and dB_z/dx) were used. These added cross terms have not been included in previous analyses of magnetic particle transport and deposition (13). However, their presence was necessary to predict the expected trajectory paths based on the measured magnetic field and local deposition profile. In addition, the aerosol particles were assumed to be carried by a laminar airstream, consistent with the calculated Reynolds number. The correspondence between the experimental data and the simulated results is quite remarkable, since no adjustable parameters were used.

Limitations of the CFD model include the assumption of a constant magnetic field in the axial (downstream) direction, the assumption of spherical aggregate particles, and the use of a single volume fraction for all particle sizes. Specifically, the magnetic field varied in the x and z directions based on experimental measurements, but was assumed constant in the y-direction. Neglecting the fringe effects is most likely why the deposition zone was much better defined in the numerical simulations compared with the *in vitro* photograph (Fig. 9). In future analyses, more complete measurements of the magnetic field will allow for the inclusion of fringe effects in the CFD model. The numerical model also assumed that the aggregate nanoparticles were spherical. SEM imaging indicates that the particles are largely spherical in shape as would be expected with the evaporation of aqueous droplets. While this may be a first-order approximation, aggregates are expected to have some shape variations. Further evaluation of the aggregate geometries is needed for the development of geometric shape factors to be used in the drag coefficient calculations. Moreover, the CFD model did not assume that additional aggregation of the particles occurred after aeroso-

lization. Finally, a single volume fraction was used for all particle sizes based on an assumed crystalline packing of the aggregated nanoparticles. This volume fraction resulted in excellent agreement with the *in vitro* results across the range of aerosol sizes considered. However, experimental verification of this volume fraction would provide added confidence that the numerical model correctly predicts the inertia of the particles. Despite these limitations, the CFD model was found to match the *in vitro* data to a high degree, which can form the basis for accurately predicting targeted deposition in the respiratory tract.

Before the developed CFD model can be applied to make predictions of *in vivo* deposition, additional parameters must be considered, such as the physiological flow field and complexity of the lung structure. First, the flow field considered in the current study is laminar without changes in direction. In contrast, it is well known that airflow in the respiratory tract is characterized by directional and velocity changes in the oropharynx (26) and larynx (27), bifurcations (20), and expanding/contracting alveoli (28). These factors create deposition from turbulent dispersion and inertial impaction. Respiratory aerosols are also known to deposit as a result of sedimentation and diffusion. Future studies are needed in more realistic geometries to demonstrate that the CFD model can capture the deposition of magnetic aerosols under the influence of a magnetic body force in conjunction with sedimentation, diffusion, and impaction mechanisms. However, previous studies by our group indicate that the CFD model with the addition of appropriate user-defined routines can effectively predict the deposition of non-magnetic aerosols in complex respiratory geometries under the influence of inertia, gravity, turbulent dispersion, and Brownian motion (20,26,27,29–34).

For the prediction of *in vivo* deposition, the complexity of the respiratory tract as a whole must also be considered. It is generally accepted that a CFD model of the entire lung is not feasible. However, CFD simulations are highly effective at generating correlations for the deposition of aerosols in lung sections as functions of available parameters, such as branch geometry, flow rate, and aerosol characteristics (26,35). It is suggested that a new correlation be developed for predicting magnetic aerosol deposition in respiratory branches as a function of aerosol properties, magnetic field strength and gradient, branch geometry, and flow rate. This correlation can then be used in conjunction with existing correlations for deposition by other mechanisms in algebraic models of lung deposition, such as the ICRP (36) or NCRP (37) models. Models that isolate deposition within specific lobes of the lung should also be considered (38). The developed whole-lung model can then be applied to predict enhanced deposition of magnetic aerosols within specific lung regions, such as an individual lung lobe on a branch-averaged basis. These predictions can be used to develop protocols for targeting deposition in specific regions of the respiratory tract.

CONCLUSION

In summary, the magnetic deposition of aerosol particles has been experimentally demonstrated and simulated with a CFD model. The excellent predictive power of the CFD model suggests that inhalation delivery systems for *in vivo* selective respiratory drug delivery can potentially be designed based on observable magnetic and aerosol properties. However, future studies are needed that evaluate aerosol deposition in more realistic respiratory geometries and that translate CFD predictions of deposition to *in vivo* conditions.

ACKNOWLEDGEMENTS

Yuanyuan Xie was partially supported by the EG Rippie Fellowship. The induced moment was measured by Yun Hao Xu under the direction of Professor Jian Ping Wang. Powerscope Inc. generously arranged for our use of the aerodynamic particle sizer on loan from TSI.

REFERENCES

1. Duguet E, Vasseur S, Mornet S, Devoisselle JM. Magnetic nanoparticles and their applications in medicine. Nanomed. 2006;1:157–68.
2. Gupta PK, Hung C. Magnetically controlled targeted chemotherapy. In: Willmott N, Daly J, editors. Microspheres and regional cancer therapy. Boca Raton: CRC; 1994. p. 71–116.
3. Stahlhofen W, Moller W. Behaviour of magnetic micro-particles in the human lung. Radiat Environ Biophys. 1993;32:221–38.
4. Choi H, Choi SR, Zhou R, Kung HF, Chen IW. Iron oxide nanoparticles as magnetic resonance contrast agents for tumor imaging via folate receptor-targeted delivery. Acad Radiol. 2004;11:996–1004.
5. Gupta AK, Naregalkar RR, Vaidya VD, Gupta M. Recent advances on surface engineering of magnetic iron oxide nanoparticles and their biomedical applications. Nanomed. 2007;2:23–39.
6. Pauwels EK, Erba P. Towards the use of nanoparticles in cancer therapy and imaging. Drug News Perspect. 2007;20:213–20.
7. Ally J, Martin B, Behrad Khamesee M, Roa W, Amirfazli A. Magnetic targeting of aerosol particles for cancer therapy. J Magn Magn Mater. 2005;293:442–9.
8. Voltairas PA, Fotiadis DI, Michalis LK. Hydrodynamics of magnetic drug targeting. J Biomech. 2002;35:813–21.
9. Pankhurst A, Connolly J, Jones S, Dobson J. Applications of magnetic nanoparticles in biomedicine. J Physics D: Appl Phys. 2003;36:167–81.
10. McCarthy JR, Kelly KA, Sun EY, Weissleder R. Targeted delivery of multifunctional magnetic nanoparticles. Nanomed. 2007;2:153–67.
11. Zhang JL, Srivastava RS, Misra RD. Core-shell magnetite nanoparticles surface encapsulated with smart stimuli-responsive polymer: synthesis, characterization, and LCST of viable drug-targeting delivery system. Langmuir. 2007;23:6342–51.
12. Brain JD, Bloom SB, Valberg PA, Gehr P. Correlation between the behavior of magnetic iron oxide particles in the lungs of rabbits and phagocytosis. Exp Lung Res. 1984;6:115–31.
13. Jang M, Cao G. Deposition of magnetic nanoparticles suspended in the gas phase on a specific target area. Environ Sci Technol. 2006;40:6730–7.
14. Martin AR, Finlay WH. Enhanced deposition of high aspect ratio aerosols in small airway bifurcations using magnetic field alignment. J Aerosol Sci. 2008;39:679–90.
15. Dames P, Bernhard G, Flemmer A, Hajek K, Seidl N, Wiekhorst F, *et al.* Target delivery of magnetic aerosol droplets to the lung. Nature Nanotechnology. 2007;2:495–9.
16. Massart R. Preparation of aqueous magnetic liquids in alkaline and acidic media. IEEE Trans Magn. 1981;17:1247–8.
17. Liao X, Liang W, Wiedmann T, Wattenberg L, Dahl A. Lung distribution of the chemopreventive agent difluoromethylornithine (DFMO) following oral and inhalation delivery. Exp Lung Res. 2004;30:755–69.
18. Vinchurkar S, Longest PW. Evaluation of hexahedral, prismatic and hybrid mesh styles for simulating respiratory aerosol dynamics. Comput Fluids. 2008;37:317–31.

19. Longest PW, Xi J. Effectiveness of direct Lagrangian tracking models for simulating nanoparticle deposition in the upper airways. Aerosol Sci Tech. 2007;41:380–97.
20. Longest PW, Vinchurkar S. Validating CFD predictions of respiratory aerosol deposition: effects of upstream transition and turbulence. J Biomech. 2007;40:305–16.
21. Morsi SA, Alexander AJ. An investigation of particle trajectories in two-phase flow systems. J Fluid Mech. 1972;55:193–208.
22. Longest PW, Kleinstreuer C, Buchanan JR. Efficient computation of micro-particle dynamics including wall effects. Comput Fluids. 2004;33:577–601.
23. Rosensweig R. Heating magnetic fluid with alternating magnetic field. J Magn Magn Mat. 2002;252:370–4.
24. Zeng P, Kline T, Wang J-P, Wiedmann T. Thermal response of superparamagnetic particles suspended in liquid and solid media. J Magn Magn Mat. 2009;321:373–6.
25. Weitz DA. Packing in the spheres. Science. 2004;303:968–9.
26. Xi J, Longest PW. Transport and deposition of micro-aerosols in realistic and simplified models of the oral airway. Ann Biomed Eng. 2007;35:560–81.
27. Xi J, Longest PW, Martonen TB. Effects of the laryngeal jet on nano- and microparticle transport and deposition in an approximate model of the upper tracheobronchial airways. J Appl Physiol. 2008;104:1761–77.
28. Haber S, Yitzhak D, Tsuda A. Gravitational deposition in a rhythmically expanding and contracting alveolus. J Appl Physiol. 2003;95:657–71.
29. Longest PW, Hindle M, Das Choudhuri S, Byron PR. Numerical simulations of capillary aerosol generation: CFD model development and comparisons with experimental data. Aerosol Sci Tech. 2007;41:952–73.
30. Longest PW, Hindle M, Das Choudhuri S, Xi J. Comparison of ambient and spray aerosol deposition in a standard induction port and more realistic mouth-throat geometry. J Aerosol Sci. 2008;39:572–91.
31. Longest PW, Oldham MJ. Mutual enhancements of CFD modeling and experimental data: a case study of one micrometer particle deposition in a branching airway model. Inhal Toxicol. 2006;18:761–72.
32. Longest PW, Vinchurkar S. Effects of mesh style and grid convergence on particle deposition in bifurcating airway models with comparisons to experimental data. Med Eng Phys. 2007;29:350–66.
33. Xi J, Longest PW. Effects of oral airway geometry characteristics on the diffusional deposition of inhaled nanoparticles. ASME J Biomech Eng. 2008;130:011008.
34. Xi J, Longest PW. Evaluation of a novel drift flux model for simulating submicrometer aerosol dynamics in human upper tracheobronchial airways. Ann Biomed Eng. 2009;36:1714–34.
35. Longest PW, Vinchurkar S. Inertial deposition of aerosols in bifurcating models during steady expiratory flow. J Aerosol Sci. 2009;40:370–8.
36. ICRP. Human respiratory tract model for radiological protection. New York: Elsevier Science; 1994.
37. NCRP. Deposition, retention and dosimetry of inhaled radioactive substances. Bethesda: National Council on Radiation Protection and Measurements; 1997.
38. Yeh HC, Schum GM. Models of human lung airways and their application to inhaled particle deposition. Bull Math Biology. 1980;42:461–80.